Large atom number Bose-Einstein condensate machines

Erik W. Streed
MIT-Harvard Center for Ultracold Atoms, Research Laboratory of Electronics, Massachusetts Institute of Technology, Cambridge, Massachusetts 02139 and Department of Physics, Massachusetts Institute of Technology, Cambridge, Massachusetts 02139

Ananth P. Chikkatur
Belfer Center for Science and International Affairs, Littauer P-14, 79 JFK Street, Harvard University, Cambridge, Massachusetts 02138

Todd L. Gustavson
Hansen Experimental Physics Laboratory End Station 3, Room M302, Department of Physics, Stanford University, Stanford, California 94305

Micah Boyd
MIT-Harvard Center for Ultracold Atoms, Research Laboratory of Electronics, Massachusetts Institute of Technology, Cambridge, Massachusetts 02139 and Department of Physics, Massachusetts Institute of Technology, Cambridge, Massachusetts 02139

Yoshio Torii
Institute of Physics, University of Tokyo, 3-8-1, Meguru-ku, Komaba, Tokyo 153-8902, Japan

Dominik Schneble
Physics A-106, Department of Physics and Astronomy, SUNY Stony Brook, Stony Brook, New York 11794

Gretchen K. Campbell, David E. Pritchard, and Wolfgang Ketterle
MIT-Harvard Center for Ultracold Atoms, Research Laboratory of Electronics, Massachusetts Institute of Technology, Cambridge, Massachusetts 02139 and Department of Physics, Massachusetts Institute of Technology, Cambridge, Massachusetts 02139

(Received 15 July 2005; accepted 12 December 2005; published online 24 February 2006)

We describe experimental setups for producing large Bose-Einstein condensates of ^{23}Na and ^{87}Rb. In both, a high-flux thermal atomic beam is decelerated by a Zeeman slower and is then captured and cooled in a magneto-optical trap. The atoms are then transferred into a cloverleaf-style Ioffe-Pritchard magnetic trap and cooled to quantum degeneracy with radio-frequency-induced forced evaporation. Typical condensates contain 20×10^6 atoms. We discuss the similarities and differences between the techniques used for producing large ^{87}Rb and ^{23}Na condensates in the context of nearly identical setups. © *2006 American Institute of Physics.*
[DOI: 10.1063/1.2163977]

I. INTRODUCTION

It has been a decade since Bose-Einstein condensation (BEC) in atomic vapors was first observed.[1,2] The transition from a classical thermal gas to a quantum-degenerate Bose-Einstein condensate occurs when the phase-space density $\rho=n\lambda_{dB}^3$ is increased to ~1, where n is the number density and λ_{dB} is the thermal de Broglie wavelength of the atoms. So in principle, getting a BEC is easy: you simply cool down the gas until the critical phase-space density is reached. In practice, the procedure is more complicated. A variety of different techniques are used to increase the phase-space density in several stages (Table I). Furthermore, each atom has different properties and requires modifications to the cooling techniques. Major work by many groups around the world has now extended these cooling techniques to an impressive number of atomic species: ^{87}Rb (Ref. 3), ^{23}Na (Ref. 4), ^{7}Li (Refs. 5 and 6), ^{1}H (Ref. 7), ^{85}Rb (Ref. 8), ^{4}He* (Refs. 9 and 10), ^{41}K (Ref. 11), ^{133}Cs (Ref. 12), ^{174}Yb (Ref. 13), and ^{52}Cr (Ref. 14). Still, ^{23}Na and ^{87}Rb are the two atoms with the most favorable properties for laser and evaporative coolings and are used most frequently.

A distinguishing characteristic of most experiments is the method in which atoms are laser cooled and then loaded into a magnetic or optical trap for evaporative cooling. Our approach at MIT employs atomic ovens and Zeeman slowing. Other approaches use variations of a vapor cell magneto-optical trap (MOT), in a double MOT configuration, surface MOT,[15] or as a source of low velocity atoms.[16,17] An important figure of merit of a BEC experiment is the number of atoms in the condensate. Large atom number allows better signal-to-noise ratios, greater tolerance against misalignments, and greater robustness in day-to-day operation. Since 1996, the MIT sodium BEC setups have featured the largest alkali condensates. Our three setups routinely produce condensates with atom numbers between 20 and 100×10^6. Since the diode lasers used to cool rubidium are less expensive than the dye lasers needed for sodium, most new groups have chosen to work with rubidium. The majority of ru-

TABLE I. Typical phase-space densities (ρ) during BEC production. Numbers given are for the ^{87}Rb apparatus.

Stage	n(/cm^3)	Temperature	Velocity[a]	ρ
Oven	10^{13}	383 K	334 m/s	10^{-14}
Thermal beam	10^{7}	n/a	334 m/s	10^{-20}
Slowed beam	10^{7}	n/a	43 m/s	10^{-18}
Loading MOT[b]	10^{10}	150 μK	210 mm/s	10^{-7}
Compressed MOT[b]	10^{11}	300 μK	300 mm/s	4×10^{-7}
Molasses[b]	10^{11}	10 μK	54 mm/s	6×10^{-5}
Magnetic trap	10^{11}	500 μK	380 mm/s	2×10^{-7}
BEC transition	3×10^{13}	500 nK	12 mm/s	2.61
Pure BEC	10^{14}	(250 nK)[c]	8.5 mm/s	(100)

[a]Most probable.
[b]Typical values, not measured separately.
[c]Chemical potential.

bidium experiments use vapor cell MOTs; however, the typical sizes of the condensates created with vapor cell MOTs are smaller than those realized with a Zeeman slower. The construction of vapor cell MOT rubidium condensate machines is extensively detailed in the complementary work of Ref. 18.

When the Center for Ultracold Atoms was created at MIT and Harvard, a major goal for the center was to create ^{87}Rb condensates with large atom number using the techniques developed for ^{23}Na condensates. The successful accomplishment of that goal is described in this article. Furthermore, we are able to discuss similarities and differences between the cooling techniques used for ^{87}Rb and ^{23}Na in the context of nearly identical systems. Our conclusion is that Zeeman slowing of an atomic beam works as well for ^{87}Rb as for ^{23}Na. The added length and therefore overall size of the vacuum apparatus may seem daunting; however, in our experience, the Zeeman slowing has proven to be a simple and reliable way to generate an intense slow beam. We present the technical details of how to build a large atom number Bose-Einstein condensate experiment with an intense Zeeman-slowed source for either atomic species.

These most recent, third-generation, sodium and rubidium experiments at MIT were both designed with an additional vacuum chamber ("science chamber") into which cold atoms can be moved using optical tweezers. The multichamber design allows us to rapidly reconfigure the experimental setup in the science chambers while keeping the BEC production chamber under vacuum. This has allowed us to perform very different experiments in rapid succession.[19–30]

II. SYSTEM OVERVIEW

Figure 1 illustrates the layout of our system. A thermal atomic beam emanates from the oven and is decelerated with the Zeeman slower. In the main chamber, the slowed atoms are captured and cooled with a six-beam MOT.[31] Before loading the Ioffe-Pritchard magnetic trap, the atoms are optically pumped into the $F=1$ hyperfine ground state. Atoms in the $F=1$, $m_F=-1$ state are weak magnetic-field seeking and are retained by their attraction to the field minimum in the center of the magnetic trap.

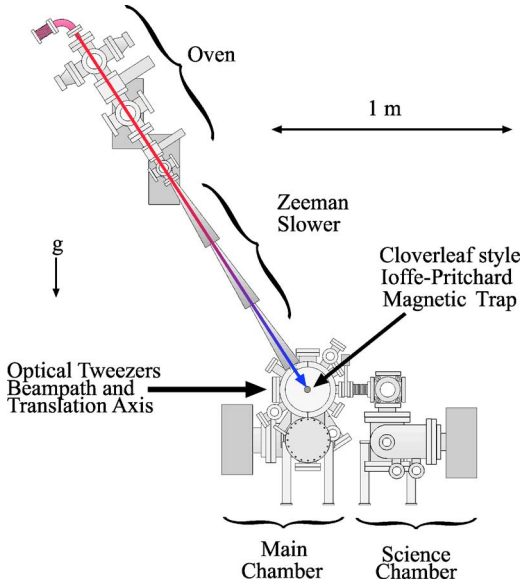

FIG. 1. (Color online) Vacuum system diagram and major subsystems. ^{87}Rb apparatus shown.

The trapped atoms are evaporatively cooled by removing hotter atoms through radio-frequency (rf)-induced transitions to untrapped states. Reducing the rf lowers the effective depth of the magnetic trap, allowing us to progressively cool to higher densities and lower temperatures until the atoms reach BEC. Magnetically trapped atoms in the $F=2$, $m_F=+2$ state have also been evaporated to BEC.

Ultracold atoms can be transported from the main chamber into the science chamber by loading the atoms into the focus of an optical tweezer and then translating the focus. In this manner we have transported ^{23}Na BECs.[19] Vibrational heating during transport cited in Ref. 19 was reduced by the use of Aerotech ABL2000 series air bearing translation stages. Technical problems related to the greater mass and higher three-body recombination rate in ^{87}Rb were overcome by transporting ultracold atoms just above the transition temperature T_c and then evaporating to BEC at the destination. The oven and Zeeman slower are tilted by 57° from horizontal to allow a horizontal orientation for the weak trapping axes of both the optical tweezers and magnetic trap.

Trapping ultracold atoms requires that they be isolated from the surrounding environment. The laser and magnetic trapping techniques confine the atoms in the center of the chamber, out of contact with the room-temperature chamber walls. The atoms are still exposed to thermal blackbody radiation but are transparent to most of the spectrum. The transitions to which the blackbody radiation can couple are the optical transitions used for laser cooling and the microwave hyperfine transitions. For optical transitions, which have energies much greater than k_BT, the excitation rate is $(3/\tau_{\mathrm{opt}})\exp(-\hbar\omega_{\mathrm{opt}}/k_BT)$, where ω_{opt} is the frequency of the transition and τ_{opt} is the lifetime of the excited state. For rubidium in a 25 °C chamber this gives a characteristic excitation lifetime of $\sim10^{11}$ yr. Raising the chamber temperature to 680 °C increases the optical excitation rate into the experimentally relevant domain of once per minute. The hyperfine transitions are significantly lower in energy compared

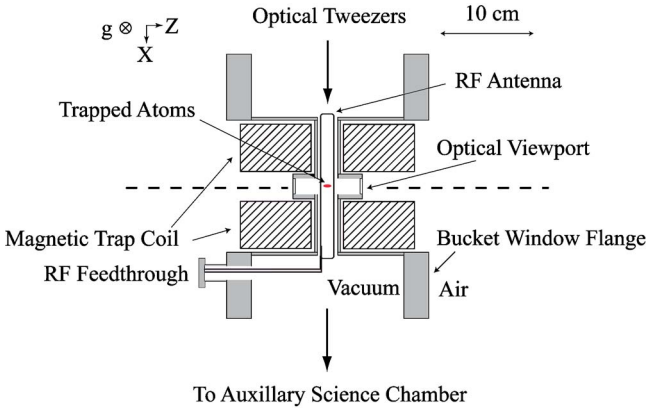

FIG. 2. (Color online) Main chamber cross section showing reentrant bucket windows, magnetic trap coils, and rf antenna. View from above.

to k_BT and have an excitation rate of $(3/\tau_{hfs})(k_BT/\hbar\omega_{hfs})$, which is once per year at 25 °C in ^{87}Rb. Neither of these excitation rates are limitations on current experiments.

Collisions with background gas molecules result in loss from the trap, necessitating low-vacuum pressure for long atom cloud lifetime. We can magnetically trap ultracold atomic clouds with lifetimes of several minutes in the $<10^{-11}$ torr ultrahigh-vacuum (UHV) environment of the main production chamber. To achieve this vacuum performance we have followed the general guidelines set out in Ref. 32 for constructing vacuum systems. The main chamber body was constructed of nonmagnetic 304 stainless steel and then electropolished to reduce the surface roughness. The only component placed inside the chamber was the rf evaporation antenna coil (Fig. 2).

The cloverleaf-style Ioffe-Pritchard magnetic trap coils fit inside two reentrant bucket windows,[33] allowing them to be outside the chamber with an intercoil spacing of 25 mm (Fig. 2). The Zeeman slower tube is mounted between the main chamber and the oven chamber. The Zeeman slower coils surrounding the Zeeman slower tube are also outside of the vacuum system but cannot be removed without breaking vacuum.

After assembling the chamber, we pumped out the system and reached UHV conditions by heating the system to accelerate outgassing. We heated the main chamber to 230 °C and the Zeeman slower to 170 °C (limited by the coil epoxy). Using a residual gas analyzer to monitor the main chamber, we "baked" until the partial pressure of hydrogen was reduced to less than 10^{-7} torr and was at least ten times greater than the partial pressure of other gases. A typical bakeout lasted between 3 and 9 days, with temperature changes limited to less than 25 °C/h. While we acknowledge the merit of using dry pumps as recommended in Ref. 18, we use oil-sealed rotary vane roughing pumps to back our turbo pumps. The vacuum in the main chamber is preserved after bakeout with a 75 L/s ion pump and a titanium sublimation pump. Refer to Sec. 3.4 of Ref. 34 for more details of our bakeout procedures.

III. OVEN

We generate large fluxes of thermal atoms for Zeeman slowing from effusive atomic beam ovens. An effusive beam is created by atoms escaping through a small hole in a heated chamber.[35] The higher vapor pressure of rubidium requires a more complicated design but lower operating temperature (110–150 °C Rb, 260–350 °C Na.) At room temperature, the vapor pressure of sodium [$\approx 3\times10^{-11}$ torr (Ref. 36)] is compatible with our UHV main chamber environment, while that of rubidium [$\approx 4\times10^{-7}$ torr (Ref. 37)] is not. This dictated that the design of the rubidium oven prevents the contamination of the main chamber with rubidium. Because of its greater complexity, further discussion will focus on the rubidium oven (Fig. 3). We expect that the rubidium oven design would also work for sodium, but instead we used a simpler design for sodium as described in Ref. 34.

A combination of active pumping and passive geometrical techniques were used to reduce extraneous rubidium transfer to the main chamber. A cold cup (I) is used to reduce rubidium vapor in the oven chamber by almost completely surrounding the oven aperture (J) with a cold surface at −25 °C. After bakeout, the combination of cold cup and oven chamber ion pump has achieved pressures as low as $\sim10^{-9}$ torr, although we have successfully made BECs with pressures of up to $\sim10^{-6}$ torr in this region. The combination of a differential pumping tube, an ion pump, and the Zeeman slower tube provides a pressure differential of over three orders of magnitude between the oven and main chamber. This is sufficient to isolate the UHV environment from an oven pressure dominated by rubidium vapor at room temperature. When the oven is opened to replace rubidium and clean the cold cup, the main chamber vacuum is isolated with a pneumatic gate valve. A second gate valve can be used in case of failure of the first. While not used in our system, designers may want to consider gate valves with an embedded window available from VAT to allow optical access along the Zeeman slower or tweezer beam lines during servicing.

The oven is loaded with a sealed glass ampoule containing 5 g of rubidium in an argon atmosphere. To add rubidium, the ampoule is cleaned, placed in the oven, and baked out under vacuum while still sealed. We then break the ampoule under vacuum and heat the oven to 110 °C to produce the atomic beam. During operation, the machine is ran as a sealed system, without the turbomechanical pump, to prevent accidental loss of the main chamber vacuum. Oven temperatures from 150 down to 110 °C produce similar-sized ^{87}Rb BECs. Reducing the oven temperature increases the time between rubidium changes to greater than 1000 h of operating time. This long operating cycle precluded the need for more complex recycling oven designs.[38]

IV. ZEEMAN SLOWER

The atomic beams are slowed from thermal velocities by nearly an order of magnitude by scattering photons from a resonant, counterpropagating laser beam. When a photon with momentum $\hbar k$ ($k=2\pi/\lambda$) is absorbed or emitted by an atom with mass m, the atom will recoil with a velocity change of $v_r=\hbar k/m$ to conserve momentum. Atoms can resonantly scatter photons up to a maximum rate of $\Gamma/2$, where $1/\Gamma=\tau$ is the excited-state lifetime. This results in a

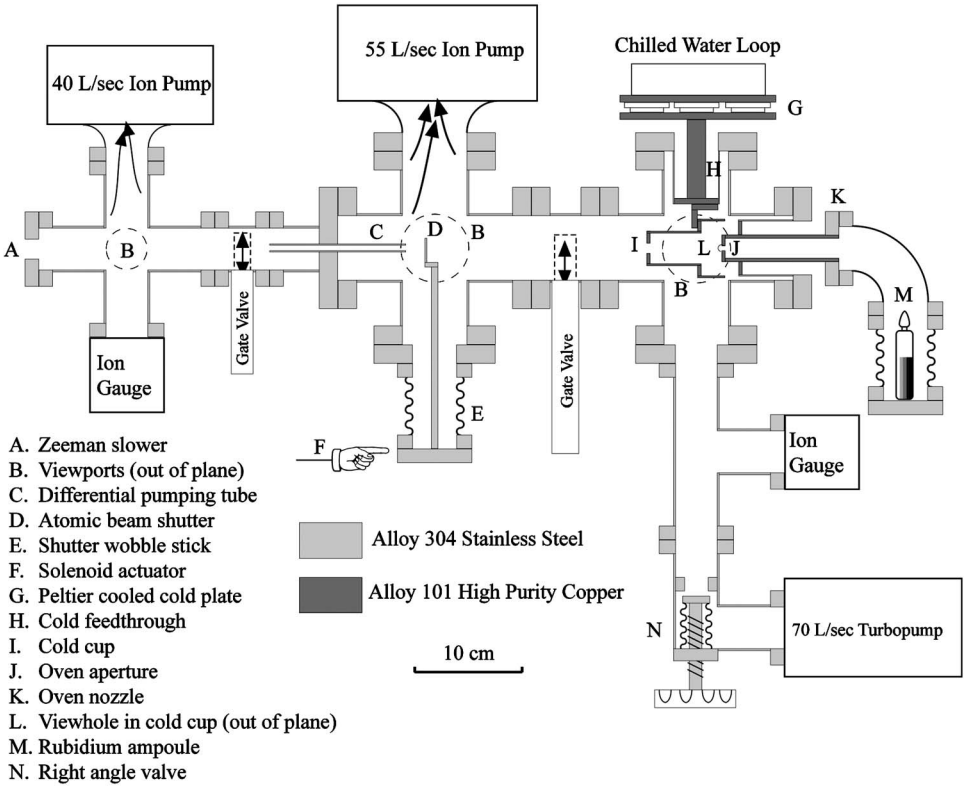

FIG. 3. Effusive rubidium beam oven. Rubidium metal (*M*) is heated to between 110 and 150 °C, creating a $p_{\mathrm{Rb}} \sim 0.5$ mtorr vapor which escapes through a 5-mm-diam hole (*J*). A 7.1-mm-diam hole in the cold cup (*I*), 70 mm from the nozzle, allows 0.3% of the emitted flux to pass through, forming an atomic beam with a flux of $\sim 10^{11}$ at./s. The remainder is mostly (99.3%) captured on the −30 °C, $p_{\mathrm{Rb}} \approx 2.5 \times 10^{-10}$ torr, surface of the Peltier-cooled cold cup. We chop this beam with a paddle (*D*) mounted to a flexible bellows (*E*). The differential pumping tube (*C*) and Zeeman slower tube (*A*) consecutively provide 170× and 620× of pressure reduction between the oven and main chambers.

maximum acceleration $a_{\max} = \hbar k \Gamma / 2m$ (1.1×10^5 m/s^2 Rb, 9.3×10^5 m/s^2 Na). As the atoms decelerate, the reduced Doppler shift is compensated by tuning the Zeeman shift with a magnetic field[39] to keep the optical transition on resonance. We designed our slowers to decelerate the atoms at a reduced rate $fa_{\max}$ where $f \sim 50\%$ is a safety factor to allow for magnetic-field imperfections and finite laser intensity.

Our slowers are designed along the lines of Ref. 40, with an increasing magnetic field and σ^--polarized light scattering off the $F=2$, $m_F=-2 \rightarrow F'=3$, $m_{F'}=-3$ cycling transition. Before the slowing begins, the atoms are optically pumped into the $F=2$, $m_F=-2$ state. The large magnetic field at the end of the slower corresponds to a large detuning from the low velocity, low magnetic field resonance frequency. This large detuning allows the slowing light to pass through the MOT without distorting it due to radiation pressure. Within the slower coils, the quantization axis is well defined by the longitudinal magnetic field, and the optical pumping out of the cycling transition is strongly suppressed by the combination of light polarization and Zeeman splitting.

We slow ^{87}Rb atoms from an initial velocity of ~350 m/s with a tailored 271 G change in the magnetic field (Fig. 4). An additional uniform ~200 G bias field was applied along the length of the slower to ensure that neighboring hyperfine levels were not near resonance in either the slower or the MOT. The slower cycling transition light is detuned −687 MHz from the $F=2 \rightarrow F'=3$ transition. The slowing laser intensity is $I/I_{\mathrm{sat}} \approx 8$, giving a maximum theoretical deceleration of 89% of $a_{\max}$. To maximize the number of atoms in the slowed $F=2$, $m_F=-2$ state "slower repumping" light copropagates with the cycling transition light and is detuned −420 MHz from the $F=1 \rightarrow F'=1$ transition to match the Doppler shift of the unslowed thermal atoms from the oven. A flux of $\sim 10^{11}$ ^{87}Rb atoms/s with a peak velocity of 43 m/s was measured from our slower with an oven temperature of 150 °C. This is a significantly greater flux than the 8×10^8 Rb/*s* vapor cell loading rate quoted by Ref. 18. Higher flux (3.2×10^{12} Rb/s) can be achieved with additional complexity, as demonstrated in Ref. 41.

The higher temperature of the sodium oven, along with the atoms' lower mass, results in a greater initial velocity of 800–950 m/s. This requires a slower with a much larger magnetic-field change of 1150 G. To reduce the maximum magnitude of the magnetic fields we use the "spin-flip" variant of the increasing field design by shifting the zero cross-

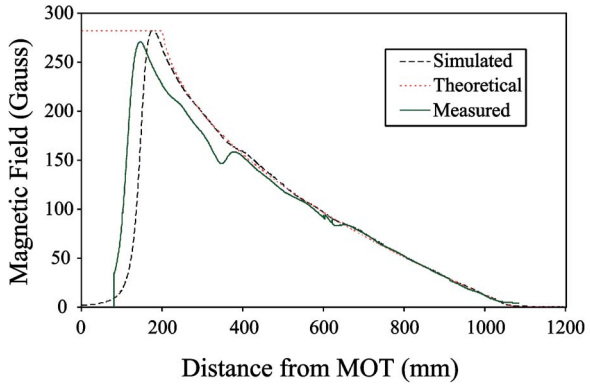

FIG. 4. (Color online) Magnetic field profile of the rubidium Zeeman slower, not including uniform bias field. The theoretical line shows the desired magnetic-field profile for atoms decelerated from 330 to 20 m/s at 60% of the maximum intensity-limited deceleration ($f=53\%$ of $a_{\max}$). The simulated line depicts the expected field from slower coils with the winding pattern in Fig. 11 of Appendix B. The prominent bumps shown above in the measured field were subsequently smoothed with additional current carrying loops.

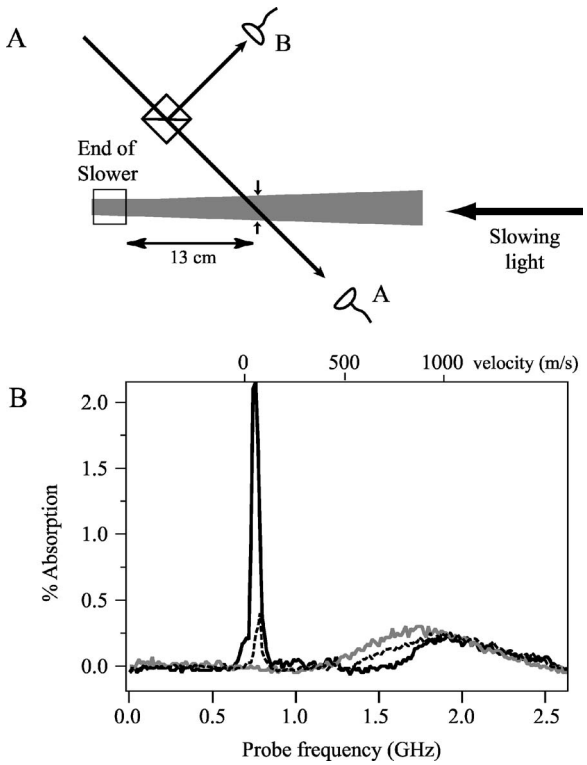

FIG. 5. Sodium slower performance. (A) Schematic of the differential absorption measurement of the slowed atomic beam. The slowed atomic beam is shown in gray. The photodiode signals *A* and *B* are subtracted and amplified. (B) Typical absorption signal for ^{23}Na beam at 45° probe angle. The black solid line is the slowed beam with both slower solenoids fully energized. The dashed line is with only the increasing field slower solenoid, and the gray line is the raw atomic beam without any slowing. The top scale converts the probe frequency into a velocity scale relative to the $F=2$ cycling transition.

ing of the magnetic field from the beginning of the slower to the middle. The first segment then becomes a decreasing field slower, with current flowing in the opposite direction of the second, increasing field segment. In the low magnetic-field region between the two segments the slowing light flips from cycling on the $F=2$, $m_F=+2$ ($m_I=+3/2$, $m_J=+1/2$ at high field) $\rightarrow F'=3$, $m_{F'}=+3$ ($m_I=+3/2$, $m_J=+3/2$) transition with σ^+ polarization to the $F=2$, $m_F=-2$ ($m_I=-3/2$, $m_J=-1/2$) $\rightarrow F'=3$, $m_{F'}=-3$ ($m_I=-3/2$, $m_J=-3/2$) transition with σ^- polarization. Similar to the rubidium slower, optical repumping light, resonant with the $F=1\rightarrow F'=2$ transition, is introduced to prepare atoms in the $F=2$, $m_F=+2$ state before slowing. In addition the repumping light protects against optical pumping into the $F=1$ manifold which may occur in the low magnetic-field region between the coils because of the small excited-state hyperfine splitting (Fig. 6). Experimentally, the absence of repumping light significantly degrades slower performance (Figs. 1-13 of Ref. 34).

The sodium slowing beam is detuned 1.0 GHz below the $F=2\rightarrow F'=3$ transition and has an intensity of $I/I_{\text{sat}}\approx 4$, giving a laser-power-limited maximum deceleration of 80% of $a_{\max}$. Unlike the rubidium slower, light for optical pumping is generated by adding 1.75 GHz sidebands to the slowing light using an electro-optical modulator. The sodium slower coils were broken up such that the first segment had an initial

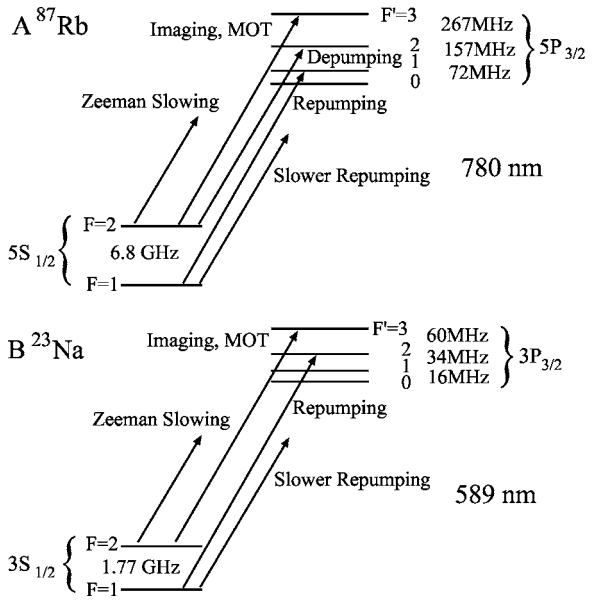

FIG. 6. Simplified level structure of ^{87}Rb (A) and ^{23}Na (B) with relevant transitions, hyperfine splittings, and laser frequencies.

field of 440 G and a length of 52 cm and the second segment had a final field of 710 G and a length of 43 cm. The sodium slower was tested as depicted in Fig. 5, with a measured flux of 3×10^{11} ^{23}Na atoms/s with a peak velocity of 100 m/s.

V. LASERS

Resonant laser light is used to slow, cool, trap, and detect the atoms. All laser light is prepared on a separate optics table and delivered to the apparatus (Fig. 1) through single-mode optical fibers. Because stray resonant light can heat the atoms during evaporation, black cloth separates the two tables. All frequency shifting and attenuation of the light is done with acousto-optic modulators. Mechanical shutters are also placed in front of each fiber coupler to block any light which might leak through the modulators and disturb the atoms. Atomic energy levels and laser frequencies used are indicated in Fig. 6.

We use different techniques for generating laser light at the resonant wavelengths of ^{87}Rb (780 nm) and ^{23}Na(589 nm). For ^{87}Rb we use a Toptica DL100 external cavity diode laser and TA100 semiconductor tapered amplifier to create 350 and 35 mW of light resonant with the ^{87}Rb $F=2\rightarrow F'=3$ and $F=1\rightarrow F'=1$ transitions at 780 nm. The lasers are stabilized with a polarization sensitive saturated absorption spectroscopy lock.[42,43] This modulation-free technique optically creates a derivative signal of the absorption spectra that is locked with a proportional-integral gain servo loop. The locking signal fluctuation indicates a frequency jitter of <1 MHz over several seconds, which is much less than the 6.1 MHz natural linewidth of ^{87}Rb. The large frequency shifts used for the slower cycling and repumping light reduced the available power to a few milliwatts. Each of these beams is amplified to 35–40 mW by injection locking[44] a free running Sanyo DL7140-201 laser diode before combining the beams on a nonpolarizing beam splitter and coupling into a fiber.

The ^{87}Rb MOT uses a total of 60 mW of light near the $F=2\rightarrow F'=3$ cycling transition for trapping/cooling. The $F=2\rightarrow F'=3$ transition in the MOT is only approximately a closed cycle, and atoms are often optically pumped into the $F=1$ ground state. To repump these atoms back into the $F=2$ state we use 10 mW of light on the $F=1\rightarrow F'=1$ transition. In addition, to transfer atoms from the $F=2$ to $F=1$ manifold, such as prior to loading them into the magnetic trap, we introduce a few milliwatts of "depumping" light resonant with the $F=2\rightarrow F'=2$ transition. Zeeman slowing uses 18 mW of slower cycling light and 6 mW of slower repumping light. All powers are quoted after fiber coupling, measured as delivered to the apparatus table.

For ^{23}Na we use a Coherent 899 dye laser pumped by a Spectra Physics Millenia laser (532 nm, 8.5 W). Typically 1.2 W of 589 nm light is generated by the dye laser. The laser frequency was referenced to an external saturation-absorption lock-in scheme and locked to a Fabry-Perot cavity. Stable operation was improved by using a precision dye nozzle (Radiant Dyes, Germany), high-pressure dye circulator at 12 bars, and stabilized temperatures for the room and dye.

For more detailed information on the generation of the laser light for sodium MOTs, see Sec. 3.4 of Ref. 45. Typical delivered laser powers are 80 mW for the MOT light, 20 mW for the repumping light, 40 mW for the slowing light and less than 1 mW for the imaging beam. Electro-optic modulators allow the addition of high-frequency sidebands ($\sim$1.8 GHz) on the slowing and MOT light for repumping without the use of an additional laser beam. Recent advances in single frequency high power fiber and diode-pumped solid-state lasers[46] have made nonlinear techniques such as sum frequency generation[47,48] and frequency doubling[49] interesting alternatives as resonant light sources.

VI. MAGNETO-OPTICAL TRAP

The MOT (Ref. 31) is the workhorse of atomic physics for creating large samples of ultracold atoms. We use a six-beam configuration, which doubles as an optical molasses when the magnetic gradient field is off. Similar to Ref. 18 the ^{87}Rb apparatus uses a bright MOT. The ^{87}Rb MOT equilibrates to around 4×10^{10} atoms after $\sim$2 s of loading, operating in a magnetic field gradient of 16.5 G/cm with cycling beams detuned -18 MHz from the $F=2\rightarrow F'=3$ transition and a peak intensity of 5.3 mW/cm^2. To increase the efficiency of the transfer into the magnetic trap, we briefly compress the ^{87}Rb MOT and then switch off the magnetic-field gradient to cool the atoms with optical molasses. The ^{87}Rb MOT is compressed by linearly ramping the gradient to 71 G/cm in 200 ms and simultaneously sweeping the detuning to -45 MHz in 400 ms. We use 5 ms of "gray" molasses, where the repumper power is dropped by 95%, the optical trapping power is ramped down to 50%, and the detuning is swept from -18 to -26 MHz. The molasses phase requires the cancellation of imbalances in intensity between beams and also of residual magnetic fields.[50] After the molasses phase, 0.5–1 ms of depumping light is applied to put all the ^{87}Rb atoms into the $F=1$ level before loading into the magnetic trap. Exact MOT and molasses parameters were found through empirical optimization, and all listed numbers should be considered as rough guides.

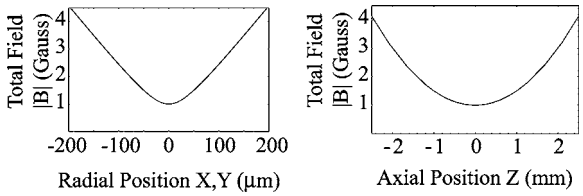

FIG. 7. Profile of the Ioffe-Pritchard trap magnetic field magnitude. The trap parameters are $B'=223$ G/cm, $B''=100$ G/cm^2, and $B_0=1$ G.

The ^{23}Na apparatus uses a dark-spot MOT,[51] with a detuning of -15 MHz, peak beam intensity of 8.8 mW/cm^2, and a magnetic-field gradient of 11 G/cm. A 4 mm diameter opaque circle blocks light in the middle of a single repumper beam, creating a region at the center of the MOT where trapped atoms are optically pumped into the $F=1$ state. The ^{23}Na MOT equilibrates after a few seconds of loading. The effectiveness of the dark-spot in ^{23}Na has precluded the need for the compression and molasses phases as in ^{87}Rb. Typically 99% of the atoms are in the $F=1$ (dark) hyperfine state.[51]

VII. MAGNETIC TRAP

Atoms in weak magnetic-field seeking states can be trapped in a magnetic-field minimum. Our magnetic trap is a high-current Ioffe-Pritchard (IP) trap with a cloverleaf-style winding that can hold $F=1$, $m_F=-1$ or $F=2$, $m_F=+2$ ground-state atoms of ^{87}Rb and ^{23}Na with long lifetimes. An IP trap has an anisotropic, "cigar"-shaped, three-dimensional (3D) harmonic shape for energies which are small compared to the trap minimum $g_F m_F \mu_B B_0$ and a two-dimensional (2D) linear/one-dimensional (1D) harmonic shape at higher energies (see Fig. 7 and Appendix C). This linear regime at higher energies (higher cloud temperatures) is more efficient for evaporatively cooling hot atoms,[52] while the finite bias field at the minimum prevents Majorana spin-flip loss of colder atoms. The similar magnetic moment of ^{87}Rb and ^{23}Na allows us to use of the same magnetic trap design, with ^{23}Na realizing double the trap frequencies of ^{87}Rb due to its lower mass.

Figure 8 shows an expanded view of the magnetic trap coils. The two sets of four cloverleaf coils create radial gradients B' along $\hat{x}$ and $\hat{y}$, while the curvature coils produce a parabolic field curvature B'' in the $\hat{z}$ direction. The curvature coils also produce a substantial bias field (Table IV, Appendix C) along $\hat{z}$, which is balanced by a roughly homogeneous field from the antibias coils, resulting in a low residual bias field B_0 of $\sim$1 G at the center of the trap. The subtraction of the large magnetic fields from the curvature and antibias coils can make the residual bias field B_0 susceptible to jitter from current noise. To prevent this we drive current through both coils in series from the same power supply (Appendix C, Fig. 12), reducing the effect of current noise in the residual bias field B_0 by $\approx$30. When assembled the antibias coils enclose the cloverleaf coils, and the MOT coils surround the curvature coils.

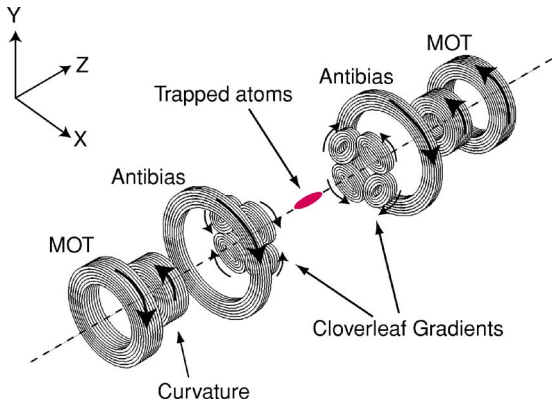

FIG. 8. (Color online) Exploded view of the cloverleaf-style Ioffe-Pritchard trap coils. Arrows indicate the direction of current flow. MOT coils are not on during magnetic trapping. Performance and design details are listed in Table IV of Appendix C.

To preserve phase-space density during the transfer of atoms into the magnetic trap, additional current is applied to the curvature coils, increasing the residual bias field and decreasing the radial confinement to make a roughly spherical magnetic trap that more closely mode matches the spherical MOT. After loading the atoms in the trap, the additional curvature coil current is reduced over 1 s to adiabatically change the trap geometry to the tightly confining cigar shape, favorable for evaporative cooling. Section 2.3.2 of Ref. 53 has an extensive discussion of mode matching magnetic traps to MOTs. The adiabatic compression technique is reviewed in Ref. 52.

VIII. CONTROL AND IMAGING

Two computers run the apparatus; one controls the various parts of experiment and the other processes images from a camera which images the atoms. The control computer has custom built National Instruments (NI) LABWINDOWS based software to drive analog (2 NI Model PCI 6713, 8 channels of 12 bit analog, 1 MS/s update) and digital output (2 NI Model PCI-6533, 32 channels of binary transistor-transistor logic (TTL), 13.3 MS/s update) boards. The control computer also controls an Agilent 33250A 80 MHz function generator through a general purpose interface bus (GPIB) interface, and triggers a Princeton Instruments NTE/CCD-1024-EB camera through a ST-133 controller to capture the absorption images.

BECs are typically imaged 10–40 ms after release from the trap. References 53 and 54 provide details for analyzing condensates after free expansion. Atoms are first optically pumped into the $F=2$ state in 200 μs, and then an absorption image is taken using resonant $F=2\rightarrow F'=3$ light. Detuning off resonance causes dispersion (lensing) as the light passes through the cloud of atoms and can distort the image. The intensity of the imaging probe is kept lower than the saturation intensity to prevent bleaching of the transition, which would lead to errors in atom number counting. Typical exposure times are between 50 and 200 μs. Section III of Ref. 53 discusses other imaging techniques that can also be used to probe BECs. Our control and imaging techniques work equally well for ^{23}Na and ^{87}Rb.

TABLE II. Select properties ^{87}Rb and ^{23}Na $F=1$, $m_F=-1$ ground states. Unless noted, quantities are derived from Refs. 36 and 69.

	^{87}Rb	^{23}Na
D_2 line λ (nm)	780	589
D_2 linewidth $\Gamma/2\pi$ (MHz)	6.1	9.8
Gravity mg/k_B(nK/μm)	102	27
Gravity $mg/g_F m_F \mu_B$(G/cm)	30	8.1
Three-body constant K_3(cm^6/s)	8×10^{-30}[a]	2×10^{-30}[b]
Scattering length a (nm)	5.3[c]	2.8[d]
Recoil velocity v_r (mm/s)	5.9	29

[a]Reference 58.
[b]Reference 60.
[c]Reference 59.
[d]Reference 68.

IX. EVAPORATION

Evaporative cooling works by selectively removing hot atoms from the trapped cloud, while the remaining atoms rethermalize to a lower temperature. The efficiency of cooling depends on η, the ratio of trap depth or energy of the escaping atoms to the temperature k_BT, and is reduced by the rate of heating. The speed of evaporation depends on how quickly the atoms rethermalize. In a magnetic trap evaporation is implemented through rf-induced transitions between trapped and untrapped states. A given rf corresponds to a shell of constant $\mu_m|\mathbf{B}|$ where the transitions occur. Atoms that pass through this shell enter untrapped states and are lost; thus rf provides a flexible mechanism to control the magnetic trap depth. Our rf antenna consists of two rectangular loops of wire, 10×2 cm, positioned 3 cm above and below the condensate as depicted in Fig. 2. Evaporation works equivalently well for ^{23}Na and ^{87}Rb, with ^{23}Na's lower mass resulting in higher trap frequencies, which roughly compensates for its smaller elastic cross section (Table II).

To evaporate thermal atoms to a BEC, we sweep the rf frequency over several seconds using an Agilent 33250A synthesizer amplified with a 5 W rf amplifier (Mini-Circuits ZHL-5W-1). Typical evaporation curves for ^{87}Rb would ramp from 60 down to ~0.8 MHz in 15–40 s, with similar parameters for ^{23}Na. Forced rf evaporative cooling is very efficient, increasing phase-space density by $>10^6$ (Table I). Figure 9 shows the drop in temperature as the trap depth

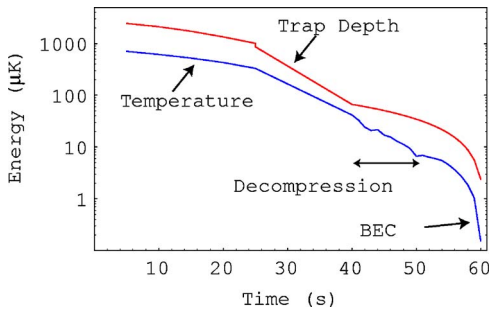

FIG. 9. (Color online) Typical temperature and trap depth during evaporation to BEC in ^{87}Rb. The trap is decompressed between $t=40$ and 50 s by changing the trap parameters $B'=223\rightarrow54$ G/cm, $B''=99\rightarrow25$ G/cm^2, and $B_0=1.4\rightarrow0.87$ G. Temperature was determined by fitting after ballistic expansion.

(calculated from the rf) is lowered during evaporation of ^{87}Rb. Evaporation curves are frequently adjusted in the interest of tuning evaporation speed, atom number, density, and/or reproducibility. For instance, the atom number can be increased by decompressing the magnetic trap near the end of the evaporation. This reduces the effects of three-body recombination heating by lowering the final condensate density. Such decompression techniques have allowed us to create nearly pure condensates with $N_c \approx 20\times10^6$ in both ^{87}Rb and ^{23}Na with lifetimes in excess of 5 s.

Decompressing the trap shifts its center due to gravitational sag and imperfections in the balance of magnetic fields between the coils. Such movements can excite oscillations in the cloud, which results in the condensation of BECs which are not at rest. Even in the absence of excitations, the magnetic-field gradients must exert a force on the atoms which is greater than gravity for them to remain trapped. This limits the extent to which magnetic traps can be decompressed. Specially designed gravitomagnetic traps have been decompressed down to 1 Hz (Ref. 22) to investigate very cold, dilute BECs.

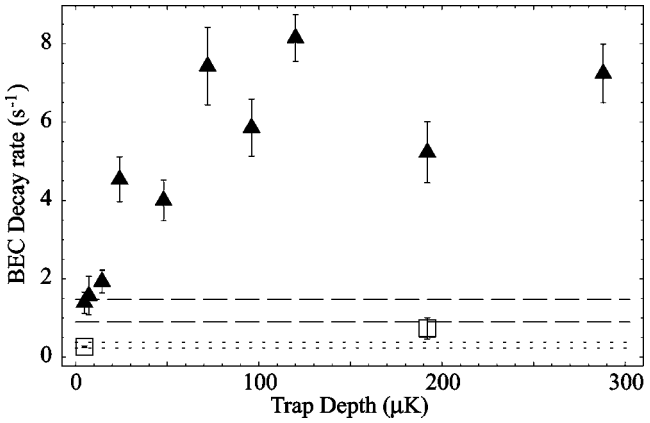

FIG. 10. Initial loss rates for ^{87}Rb BEC in deep traps. Trap depth dependence of the loss for large and small ^{87}Rb BECs in a $220\times220\times9$ Hz magnetic trap. The trap depth was controlled by rf truncation. Condensates were nearly pure ($N_c/N>90\%$) and consisted of $F=1$, $m_F=-1$ atoms. Solid triangles are data for a large condensate, $N_c=2.7\times10^6$ atoms, peak density $n_p=6.1\times10^{14}/\mathrm{cm}^3$, expected three-body decay time $\tau_3=0.85\pm0.22$ s (dashed horizontal lines) (Ref. 58), and calculated collisional opacity of 0.88 (Ref. 56). Open squares are data for a small condensate, $N_c=5\times10^5$ atoms, peak density $n_p=3.1\times10^{14}/\mathrm{cm}^3$, expected three-body decay time $\tau_3=3.3\pm0.8$ s (dotted horizontal lines), and a calculated collisional opacity of 0.32. The error bars represent the statistical uncertainity in the decay curves. Additional scatter in the data is due to fluctuations in the atom number.

X. DEEP TRAP LIMITATIONS

A major difference we have observed between ^{87}Rb and ^{23}Na condensates is the unexpectedly high decay rate of ^{87}Rb condensates in tightly confining deep traps, such as those used for transport in an optical tweezer.[19] At typical densities of condensates, the lifetime and heating are usually dominated by three-body recombination decay. However, the factor of 4 difference in the three-body rate coefficients (Table II) was insufficient to explain this major discrepancy in behavior. Three-body recombination results in a diatomic molecule and an atom which fly apart with a total kinetic energy equal to the binding energy of the diatomic molecule in the highest vibrational state. This binding energy can be estimated from the scattering length as $E_0 \sim \hbar^2/ma^2$ (Ref. 55) ($\sim$200 μK in ^{87}Rb, $\sim$2.7 mK in ^{23}Na).

We investigated this issue in a magnetic trap instead of an optical trap. While it is easier experimentally to create tight trapping and hence high densities in an optical trap, both the trap frequencies and trap depth are functions of the optical power. This makes it difficult to separate density-dependent effects, which are strongly affected by the trap frequency, from trap depth effects. In contrast, in a magnetic trap the trap depth can be controlled independently of the trap frequencies by adjusting the rf which flips atoms to untrapped states.

There are two possible processes, both involving secondary collisions, which can greatly enhance the heating and losses due to the primary three-body collisions. The first process is collisional avalanches, similar to a chain reaction, where the energetic products of three-body recombination collide with additional atoms while leaving the condensate. This process depends on the collisional opacity $\sim n\sigma l$, where $\sigma=8\pi a^2$ is the atom-atom scattering cross section, and should increase dramatically when the condensate exceeds the critical opacity of 0.693.[56] This process occurs entirely within the condensate volume and hence is independent of trap depth.

The second process can already occur at lower collisional opacities and relies on the retention of primary or secondary collision products by the trap in the so-called Oort cloud.[53,57] The retention of these atoms in the trap can cause heating and loss in the condensate as they oscillate through the condensate volume. The retention of collision products in the Oort cloud should depend on whether the trap depth is larger or smaller than their energies.

Figure 10 shows the initial loss rates measured for a large and a small BEC as a function of the magnetic trap depth. At low trap depths (5 μK) both the large and small condensate decay rates are in agreement with established three-body recombination rates.[58] Therefore, the avalanche effect does not significantly contribute to the observed decay rate, although the calculated collisional opacity for the larger condensate was 0.88 and may not be far away from the onset of avalanches. In Ref. 56 evidence for avalanches was observed at a collisional opacity of 1.4.

At high trap depths, the decay rate strongly increases for larger condensates and shortens the lifetime to less than 150 ms. In contrast, at low trap depths the large condensate had a lifetime of greater than 800 ms, in agreement with the expected losses from three-body decay. For trap depths greater than $\sim$50 μK the large ^{87}Rb condensate decay rate saturates, suggesting a maximum Oort energy.

We speculate that this enhancement of three-body related losses was not observed in ^{23}Na for several reasons. The primary decay products are monoenergetic and will escape unless the trap depth is greater than their kinetic energy (minimum of $\sim$70 μK for ^{87}Rb, $\sim$900 μK for ^{23}Na). On their way out of the condensate volume, some of the primary

three-body decay products will collide with additional condensate atoms. In ^{23}Na the elastic-scattering cross section σ is 3.6 times smaller than for ^{87}Rb, making these secondary collisions less likely. The products of such secondary collisions have a range of energies. In ^{23}Na these secondary products will typically have much higher energies, reducing their chance of remaining in the trap. In addition, the retained Oort particles need to collide with the condensate to cause additional loss. These subsequent collisions can further populate the Oort cloud.

For traps whose depths are in the intermediate region, below the minimum energy of the primary three-body recombination products, the combination of greater primary three-body decay rate, greater collision opacity, and greater fraction of secondary products retained by the Oort cloud lead to an estimated loss rate several orders of magnitude higher for ^{87}Rb than for ^{23}Na in condensates of similar sizes and densities.

The restricted optical access (Fig. 2) of our experiments limits the longitudinal (tweezer axis) trap frequency per unit trap depth. This requires optical trap depths for transporting condensates in our systems that are a significant fraction of the primary ^{87}Rb decay product energy, but a small fraction of that for ^{23}Na. Therefore ^{23}Na condensates can be easily transported using optical tweezers. For ^{87}Rb the preferred method is to transport a cloud at temperatures just above condensation, where the density is lower, and evaporate to BEC after transport.

XI. DISCUSSION

We have constructed ^{87}Rb and ^{23}Na Bose-Einstein condensate machines with nearly identical designs. In this section we highlight differences in their performance and operation. Key properties of the two species are highlighted in Table II. The four principal differences are their vapor pressure, resonant wavelength, recoil velocity, and collisional properties.

The high vapor pressure of rubidium allows oven operation at lower temperatures but requires a more elaborate oven geometry to avoid deposition of rubidium on surfaces of the main UHV chamber. The lower vapor pressure of sodium requires a higher oven operating temperature to produce comparable flux. In a Zeeman slower the stopping length L for the most probable velocity in a thermal beam is $L = 3k_B T/\hbar k\Gamma$, assuming the maximum spontaneous light force. Resonant sodium light, with a shorter wavelength and larger natural linewidth, exerts a greater spontaneous light force than in rubidium. In our systems the gain from the greater light force in sodium is balanced out by the higher operating temperatures required of the sodium oven to produce comparable flux, resulting in both the rubidium and sodium slower being about 1 m in length.

The spontaneous emission of slowing photons adds a random, diffuse velocity to the atoms as they are slowed. Due to the higher recoil velocity and greater deceleration, the slow ^{23}Na beam has a larger divergence than the ^{87}Rb beam. By keeping the distance between the end of the ^{23}Na slower and the MOT to a minimum, we maximize the transfer of atoms from the slower to the MOT. Our setup for ^{87}Rb was almost identical, but we expect that the requirement of keeping the slower and the MOT close could be relaxed. Although we have not tried it, we expect that our ^{87}Rb experiment would work for ^{23}Na with increased slower coil current but without changes to the oven, vacuum, or magnet designs.

On the laser side, a major difference is the availability of low cost high power laser diodes in the near infrared region around 780 nm. In our experience a well-ran dye laser system can provide similar performance to a diode laser system with several master and slave lasers. However, occasionally dye lasers require major maintenance in terms of dye changes or full optical realignment. An advantage in sodium is the visibility of the laser light and the atomic fluorescence. The near-infrared 780 nm light is only modestly visible, whereas the sodium line at 589 nm is near the peak of human eye sensitivity and allows fine alignments of the laser beams and the magneto-optical trap without cameras, IR cards, or IR viewers.

^{87}Rb has favorable properties for laser cooling and atom interferometry because of its greater mass, lower recoil velocity, and larger excited-state hyperfine structure. While greater mass and longer resonant wavelength give ^{133}Cs an even lower recoil velocity, its complicated collisional behavior at low magnetic fields makes it difficult to cool to BEC.[12] The lowest molasses temperature in rubidium is a factor of 10 lower than that for sodium. However, in BEC experiments the laser cooling is optimized for large atom numbers and high initial elastic collision rates in the magnetic trap, and not for the lowest temperature. For laser cooling sodium at high atom numbers, the dark spot technique[51] is crucial to avoid rescattering of light in the MOT, whereas it is not necessary in rubidium experiments. At the end of the day, although with somewhat different techniques, laser cooling works equally well for both atoms.

Both atomic species have favorable collisional properties for evaporative cooling. The elastic-scattering cross section of ^{87}Rb atoms at low temperature is four times higher than that of ^{23}Na. However, elastic collision rates after laser cooling are comparable since ^{23}Na atoms have a higher velocity for a given temperature. An advantage of ^{87}Rb is that the two ground electronic state hyperfine levels have similar scattering lengths, which can be advantageous for studies on spinor condensates and atomic clock transitions. Also, spin relaxation between the two hyperfine levels is almost completely suppressed. Mixtures of $F=1$ and $F=2$ ^{87}Rb atoms can be kept for seconds,[59] whereas in ^{23}Na they decay in milliseconds.[60] Both atoms have several Feshbach resonances below 1100 G,[61–63] but ^{87}Rb has the disadvantage that the widest known resonance is only 200 mG wide compared to 1 G for ^{23}Na and thus requires more stable magnetic fields. Another limitation is the higher rate of three-body collisions for ^{87}Rb atoms. As we discussed in Sec. X, this imposes limitations on trapping and manipulating dense ^{87}Rb condensates.

In this article, we have presented details for designing BEC machines with high performance and flexibility, and we hope that this description is useful for designing new experiments. Given the recent developments in the field, there is

TABLE III. Oven design parameters.

	Rb				Na			
Temp (°C)	Velocity[a] (m/s)	Pressure[b] (Torr)	Total flux[c] #/s	Lifetime[d] (h)	Velocity[a] (m/s)	Pressure[e] (Torr)	Total flux[c] #/s	Lifetime[f] (h)
−30	266	2.5*E*−10	1.4*E*+10	⋯	513	1.9*E*−15	2.0*E*+05	⋯
0	282	2.0*E*−08	1.1*E*+12	⋯	544	5.7*E*−13	5.8*E*+07	⋯
25	295	4.0*E*−07	2.0*E*+13	⋯	569	2.8*E*−11	2.7*E*+09	⋯
39.3[g]	302	1.8*E*−06	8.8*E*+13	⋯	582	1.9*E*−10	1.8*E*+10	⋯
90	325	1.2*E*−04	5.4*E*+15	1814	628	5.3*E*−08	4.7*E*+12	⋯
97.8[h]	329	2.0*E*−04	9.1*E*+15	1070	634	1.1*E*−07	9.6*E*+12	⋯
110	334	4.5*E*−04	2.0*E*+16	489	645	3.3*E*−07	2.9*E*+13	⋯
120	339	8.3*E*−04	3.7*E*+16	267	653	7.9*E*−07	6.8*E*+13	⋯
130	343	1.5*E*−03	6.5*E*+16	151	661	1.8*E*−06	1.5*E*+14	⋯
140	347	2.6*E*−03	1.1*E*+17	87	669	4.0*E*−06	3.4*E*+14	⋯
150	351	4.4*E*−03	1.9*E*+17	52	677	8.6*E*−06	7.1*E*+14	⋯
160	355	7.3*E*−03	3.1*E*+17	32	685	1.8*E*−05	1.5*E*+15	⋯
230	383	1.5*E*−01	⋯	⋯	739	1.6*E*−03	1.2*E*+17	1487
240	387	2.1*E*−01	⋯	⋯	746	2.9*E*−03	2.2*E*+17	845
250	391	3.0*E*−01	⋯	⋯	753	5.0*E*−03	3.7*E*+17	486
260	394	4.1*E*−01	⋯	⋯	760	8.7*E*−03	6.4*E*+17	283
340	423	4.0*E*+00	⋯	⋯	815	5.2*E*−01	⋯	⋯
350	426	5.1*E*+00	⋯	⋯	822	8.3*E*−01	⋯	⋯
360	430	6.5*E*+00	⋯	⋯	829	1.3*E*+00	⋯	⋯

[a]Most probable, 3D Beam, Sec. 5.2 of Ref. 70.
[b]Reference 37.
[c]5 mm aperture.
[d]5 g Rb.
[e]Reference 36.
[f]25 g Na.
[g]Melting point Rb.
[h]Melting point Na.

more than enough room for new experiments to join in the exploration of atom optics and many-body physics with quantum-degenerate atomic gases.

ACKNOWLEDGMENTS

Funding for the ^{87}Rb machine was provided by the NSF MIT-Harvard Center for Ultracold Atoms. Funding for the ^{23}Na machine came from NSF, the ARO MURI program, NASA, and the ONR. The authors thank S. Gupta, A. Görlitz, and A. E. Leanhardt for their contributions to the construction of the ^{23}Na machine; J. C. Mun and P. Medley for ongoing contributions to the ^{87}Rb machine; and MIT UROP students P. Gorelik and X. Sun for various contributions to the ^{87}Rb machine. The authors would also like to thank M. Saba and D. Kielpinski for critical reading of this manuscript.

APPENDIX A: OVEN

To sustain a high-flux atomic beam, the background vacuum pressure must be low enough that the mean free path between collisions is much greater than the length of the beam. To generate an effusive beam with a thermal distribution of velocities, the size of the hole through which the atoms escape must be smaller than the mean free path inside the oven. We observed in sodium that at higher pressures (e.g., temperatures) the flux of slowable atoms does not increase and the velocity distribution narrows. This phenomenon is well understood[35] and limits the flux of slow atoms from a single aperture oven.

During servicing, a clean ampoule is essential for rapid recovery of good vacuum pressure. The ampoule is cleaned by submerging it in a 50/50 mixture by volume of acetone and isopropanol for 20 min, air drying it. This removes most of the water from the glass surface, which would otherwise require more time to pump away. In the rubidium experiment the cleaned ampoule is placed in the oven while still sealed and baked for 24 h under vacuum at 150–180 °C to remove the remaining contaminates before it is broken.

To prevent accumulation of metal at the aperture (Fig. 3, *J*), the oven nozzle temperature (Fig. 3, *K*) is kept higher (~10 °C in rubidium and ~90 °C in sodium) than the rest of the oven. The velocity distribution of the beam is determined by the nozzle temperature (Fig. 3, *K*). On the other hand, the vapor pressure in the oven, which controls the beam flux, is dominated by the coldest spot in the elbow and bellows. The factor of 2 discrepancy between the observed and calculated (Table III) rubidium oven lifetimes at 110 °C can be accounted for by a spot ~10 °C colder than the lowest-measured oven temperature. The specifics of this cold spot depend on how the oven is insulated.

APPENDIX B: ZEEMAN SLOWER

Every photon which scatters off an atom to slow the atom is radiated in a random direction, increasing the atoms' spread in transverse velocity. The beam emerging from the

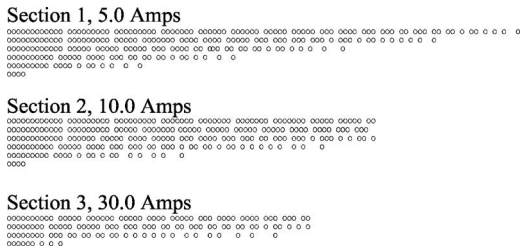

FIG. 11. Winding pattern cross section for the ^{87}Rb Zeeman slower consisting of three solenoids. Each drawing represents half of the cross section of each a solenoid. The "O"s represent wires, while the spaces between the wires were meant to be smoothed out to an average value during construction. Each character in the drawing represents a physical size of 3.5 mm. The wire is hollow core water-cooled copper, identical to that used in construction of the magnetic trap as described in Appendix C 3. The high current coil is closest to the main chamber. The single layer uniform bias coil is not depicted.

tube needs to have sufficient forward mean velocity to load the MOT efficiently. Because of the random direction of the emission recoil, N photon scatterings increase the transverse velocity by $v_r\sqrt{N/3}$. The ^{23}Na slower operates with a recoil-induced transverse exit velocity of ≈ 3 m/s, at a final forward velocity of 30 m/s so that the spatial transverse spread in the slowed beam matches the MOT capture area. The smaller initial and recoil velocities in the ^{87}Rb slower reduce the transverse velocity to ≈ 0.8 m/s, resulting in a more collimated slowed beam whose transverse width is smaller than the size of the MOT beams.

An additional concern in both slowers is the fate of atoms not captured by the MOT. In ^{87}Rb we were concerned with the potential adverse impact a deposited film may have on the vapor pressure and installed a cold plate near the slower window on the main chamber to capture desorbed Rb. Vacuum pressure has not been an issue, and we have never needed to chill this cold plate. The opposite problem arises in ^{23}Na, where metal deposition on the slower window reduces the transmission of slower light. We have found that heating the slowing beam vacuum port window to 90 °C prevents long term buildup.

1. Slower construction

The vacuum portion of the ^{87}Rb slower is a 99-cm-long nonmagnetic 304 stainless-steel tube with a 19 mm optical density (OD) and 0.9 mm wall. The rear end of the tube is connected to the main chamber by a DN 16 CF rotatable flange, while the oven end of the tube has a narrow, 50-mm-long flexible welded bellows ending in another DN 16 CF rotatable flange. The retaining ring on this flange was cut in half for removal, so that the premounted coil assembly could be slid over the vacuum tube.

As shown in Fig. 1 the slower tube enters the main chamber at an angle of 33° from the vertical to accommodate access for optical tweezers. The oven and the Zeeman slower are supported 2 m above the experimental table in order to preserve the best optical and mechanical access to the main chamber. Aluminum extrusion from 80/20 Inc. was used to create the support framework.

Our ^{87}Rb slower was fabricated with a single layer bias solenoid and three increasing field coils (Figs. 1 and 11),

TABLE IV. Magnetic trap coil winding and performance specifications. Figure 8 illustrates their assembly and direction of current flow.

Coil	Winding Turns	Winding Layers	Current (A)	Inner ∅ (cm)	Field
Antibias	3	6	95	10.5	$B''=+9$ G/cm^2 $B_0=-243$ G
Curvature	8	6	95	3.2	$B''=+90$ G/cm^2 $B_0=+251$ G
Gradient	3	4	470	0.8×2.3	$B'=223$ G/cm
MOT	7	4+2[a]	15	~7, to fit	16.5 G/cm in $\hat{z}$

[a]Segmented for improved cooling.

segmented for better cooling. The optimum configuration of currents and solenoid winding shapes was found by computer-simulated winding of the solenoids one loop at a time, starting at the high-field end and tapering the last few loops to best match the desired field profile. An alternative fabrication technique would be to apply a large uniform bias field and subtract away unwanted field with countercurrent coils. Residual field from the Zeeman slower can have a detrimental effect on the MOT, shifting its location suddenly during turnoff. A coil canceling out the residual bias field of the slower at the MOT center is installed on the ^{23}Na machine but absent on the ^{87}Rb machine. While not essential, it simplifies operation of the machine.

APPENDIX C: MAGNETIC TRAP

1. Ioffe-Pritchard trapping potential

The field near the minimum of an Ioffe-Pritchard trap is approximately

$$\mathbf{B} = B_0\begin{pmatrix}0\\0\\1\end{pmatrix} + B'\begin{pmatrix}x\\-y\\0\end{pmatrix} + \frac{B''}{2}\begin{pmatrix}-xz\\-yz\\z^2-\frac{1}{2}(x^2+y^2)\end{pmatrix}, \tag{C1}$$

which realizes trap frequencies,

$$m\omega_{x,y}^2 = \mu_m(B'^2/B_0), \tag{C2}$$

$$m\omega_z^2 = \mu_m B''. \tag{C3}$$

Typical trap parameters of $B'=223$ G/cm, $B''=100$ G/cm^2, $B_0=1$ G (Fig. 7, Table IV) have frequencies of $(\omega_{x,y},\omega_z)/2\pi$ of (200,9) Hz for ^{87}Rb and (390,18) Hz for ^{23}Na. Further details of the Ioffe-Pritchard magnetic traps are discussed in Sec. 2.3.2 of Ref. 53 and Chap. 5. of Ref. 64. A general overview of magnetic trapping can be found in Ref. 65.

2. Circuitry

Figure 12 is representative of the magnetic trap circuit. We drive the magnetic trap coils with Lambda EMI dc power supplies in fixed current mode. Current to the cloverleaf coils is supplied from a Model ESS 30-500 15 kW power supply,

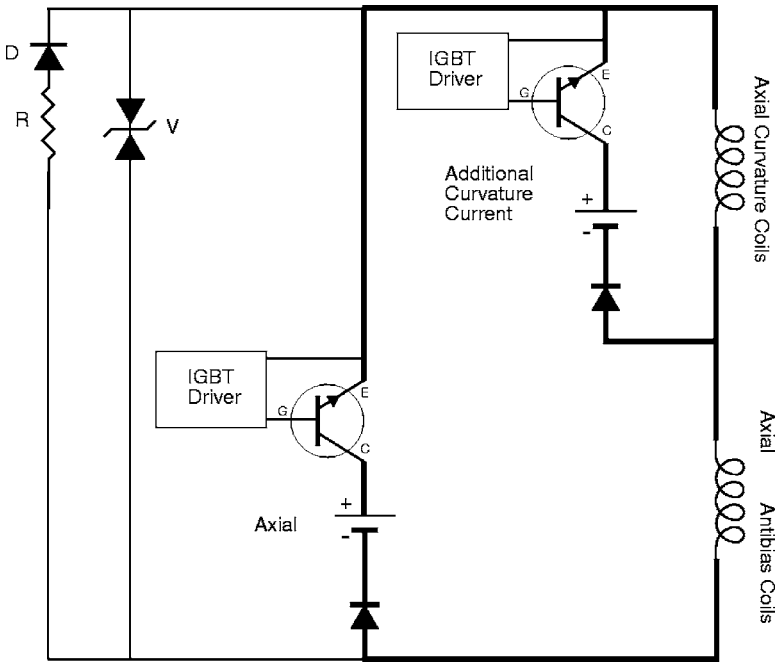

FIG. 12. Axial coil circuit diagram. High-current wires are heavy black lines.

while the axial currents are driven with two Model EMS 20-250 5 kW power supplies. Each power supply is protected against damage from reverse current with an International Rectifier SD600N04PC high-current diode.

To switch the high currents we use PowerEx models CM1000HA-24H and CM600HA-24H integrated gate bipolar transistors (IGBTs) controlled with PowerEx BG1A-F IGBT driver kits. The IGBTs and high-current diodes dissipate several hundred watts during operation and are cooled with chilled water. Efficient heat sinking is critical for reliable operation, as thermal dissipation limits the maximum dc current. Fast turnoff of current on an inductive load, such as a coil, results in a large voltage spike. We have added a "debounce" circuit to each of the coil systems (Fig. 12) to control this process and prevent damage. The circuit consists of two different elements: a varistor (V) and a diode (D) in series with a low impedance resistor (R). The varistor shorts the circuit at high voltages to prevent this spike, and the diode (D) in series with a 1 Ω resistor (R) dissipates the remaining current after varistor shutoff. Reference 66 contains a thorough analysis of the behavior of a similar circuit. All control signals are electrically isolated from the high-current circuits to prevent voltage spikes from damaging connected hardware. Rapid, controlled magnetic-field shutoff is important for quantitative interpretation of images taken after ballistic expansion.

3. Wire

Both the slower and the magnetic trap coils were fabricated using square hollow core (0.125 in./side, 0.032 in. wall) Alloy 101 soft temper copper tubing from Small Tube Products, Inc. of Altoona, PA, wrapped with double Dacron glass fuse insulation by Essex Group Inc., Magnet Wire & Insulation of Charlotte, NC. The coils are held together with Hysol Epoxi-Patch 1C White high-temperature epoxy that is bakable to 170 °C. Chilled water is forced through the hollow core of the copper wires to dissipate ≈10 kW of power generated from resistive heating in the magnetic trap and Zeeman slower coils. A differential pressure of 200 psi is required for sufficient coolant flow. We designed all our coils to increase the cooling water temperature by less than 50 °C. Chapter 3 of Ref. 67 has an extensive discussion of water cooling in continuously powered resistive magnets. For our wire the following empirical relationships and numbers were measured:

$$\rho[\Omega/\mathrm{m}] = 2.65 \times 10^{-3}, \tag{C4}$$

$$Q[\mathrm{ml/s}] = 2.07\sqrt{\frac{\Delta P[\mathrm{psi}]}{L[\mathrm{m}]}}, \tag{C5}$$

$$\Delta T[^{\circ}\mathrm{C}] = 259 I^2[\mathrm{A}]\rho\sqrt{\frac{L^3[\mathrm{m}]}{\Delta P[\mathrm{psi}]}}, \tag{C6}$$

where Q is the water flow rate in ml/s, $I^2\rho L$ is the power dissipated by the coil, ΔP the pressure drop in psi (1 psi =6.89 kPa), and L the length of the coil in meters.

4. Fabrication

All of the components for each half of the magnetic trap were epoxied together for stability. Each assembly was then mounted in the bucket windows with an aluminum mounting plate backed by four threaded Alloy 316 stainless-steel rods. No ferromagnetic materials were used in the mounting because of concern for irreproducibility from hysteresis effects. Table IV lists the windings and typical parameters for each coil.

[1] E. A. Cornell and C. E. Wieman, Rev. Mod. Phys. **74**, 875 (2002).
[2] W. Ketterle, Rev. Mod. Phys. **74**, 1131 (2002).
[3] M. H. Anderson, J. R. Ensher, M. R. Matthews, C. E. Wieman, and E. A. Cornell, Science **269**, 198 (1995).
[4] K. B. Davis, M.-O. Mewes, M. R. Andrews, N. J. van Druten, D. S. Durfee, D. M. Kurn, and W. Ketterle, Phys. Rev. Lett. **75**, 3969 (1995).

[5] C. C. Bradley, C. A. Sackett, J. J. Tollett, and R. G. Hulet, Phys. Rev. Lett. **75**, 1687 (1995); Phys. Rev. Lett. **79**, 1170 (1997).
[6] C. Bradley, C. Sackett, and R. Hulet, Phys. Rev. Lett. **78**, 985 (1997).
[7] D. Fried, T. Killian, L. Willmann, D. Landhuis, S. Moss, D. Kleppner, and T. Greytak, Phys. Rev. Lett. **81**, 3811 (1998).
[8] S. Cornish, N. Claussen, J. Roberts, E. Cornell, and C. Wieman, Phys. Rev. Lett. **85**, 1795 (2000).
[9] A. Roberts *et al.*, Science **292**, 461 (2001).
[10] F. Santos *et al.*, Phys. Rev. Lett. **86**, 3459 (2001).
[11] G. Modugno, G. Ferrari, G. Roati, R. Brecha, A. Simoni, and M. Inguscio, Science **294**, 1320 (2001).
[12] T. Weber, J. Herbig, M. Mark, H. Nagerl, and R. Grimm, Science **294**, 232 (2003).
[13] Y. Takasu *et al.*, Phys. Rev. Lett. **91**, 040404 (2003).
[14] A. Griesmaier, J. Werner, S. Hensler, J. Stuhler, and T. Pfau, Phys. Rev. Lett. **94**, 160401 (2005).
[15] H. Ott, J. Fortagh, G. Schlotterbeck, A. Grossmann, and C. Zimmermann, Phys. Rev. Lett. **87**, 230401 (2001).
[16] K. Dieckmann, R. J. C. Spreeuw, M. Weidemüller, and J. T. M. Walraven, Phys. Rev. A **226**, 58 (1998).
[17] R. S. Conroy, Y. Xiao, M. Vengalattore, W. Rooijakkers, and M. Prentiss, Opt. Commun. **226**, 259 (2003).
[18] H. Lewandowski, D. Harber, D. Whitaker, and E. Cornell, J. Low Temp. Phys. **132**, 309 (2003).
[19] T. Gustavson, A. Chikkatur, A. Leanhardt, A. Görlitz, S. Gupta, D. Pritchard, and W. Ketterle, Phys. Rev. Lett. **88**, 020401 (2002).
[20] A. E. Leanhardt, A. P. Chikkatur, D. Kielpinski, Y. Shin, T. L. Gustavson, W. Ketterle, and D. E. Pritchard, Phys. Rev. Lett. **89**, 040401 (2002).
[21] A. P. Chikkatur *et al.*, Science **296**, 2193 (2002).
[22] A. E. Leanhardt *et al.*, Science **301**, 1513 (2003).
[23] A. E. Leanhardt, Y. Shin, A. P. Chikkatur, D. Kielpinski, W. Ketterle, and D. E. Pritchard, Phys. Rev. Lett. **90**, 100404 (2003).
[24] Y. Shin *et al.*, Phys. Rev. Lett. **93**, 160406 (2004).
[25] T. Pasquini, Y. Shin, C. Sanner, M. Saba, A. Schirotzek, D. Pritchard, and W. Ketterle, Phys. Rev. Lett. **93**, 223201 (2004).
[26] Y. Shin, M. Saba, A. Schirotzek, T. A. Pasquini, A. E. Leanhardt, D. E. Pritchard, and W. Ketterle, Phys. Rev. Lett. **92**, 150401 (2004).
[27] Y. Shin, M. Saba, T. Pasquini, W. Ketterle, D. Pritchard, and A. Leanhardt, Phys. Rev. Lett. **92**, 050405 (2004).
[28] D. Schneble, Y. Torii, M. Boyd, E. Streed, D. E. Pritchard, and W. Ketterle, Science **300**, 475 (2003).
[29] D. Schneble, G. K. Campbell, E. W. Streed, M. Boyd, D. E. Pritchard, and W. Ketterle, Phys. Rev. A **69**, 041601 (2004).
[30] G. Campbell, A. Leanhardt, J. Mun, M. Boyd, E. Streed, W. Ketterle, and D. Pritchard, Phys. Rev. Lett. **94**, 170403 (2005).
[31] E. Raab, M. Prentiss, A. Cable, S. Chu, and D. Pritchard, Phys. Rev. Lett. **59**, 2631 (1987).
[32] J. O'Hanlon, *A User's Guide to Vacuum Technology* (Wiley-Interscience, Hoboken, NJ, 1989).
[33] Simon Hanks of UKAEA, D4/05 Culham Science Center, Abingdon, UK.
[34] A. P. Chikkatur, Ph.D. thesis, Massachusetts Institute of Technology, 2002; http://cua.mit.edu/ketterle_group/Theses/thesis_APC.pdf
[35] H. Pauly and C. Scoles, *Atomic and Molcular Beam Methods* (Oxford University Press, Oxford, 1988), Vol. 1.
[36] D. Steck, http://steck.us/alkalidata/sodiumnumbers.pdf (2003).
[37] C. Alcock, V. Itkin, and M. Horrigan, Can. Metall. Q. **23**, 309 (1984).
[38] M. Walkiewicz, P. Fox, and R. Scholten, Rev. Sci. Instrum. **71**, 3342 (2000).
[39] W. Phillips and H. Metcalf, Phys. Rev. Lett. **48**, 596 (1982).
[40] T. Barrett, S. Daporeschwartz, M. Ray, and G. Lafyatis, Phys. Rev. Lett. **67**, 3483 (1991).
[41] C. Slowe, L. Vernac, and L. V. Hau, Rev. Sci. Instrum. **76**, 103101 (2005).
[42] Y. Yoshikawa, T. Umeki, T. Mukae, Y. Torii, and T. Kuga, Appl. Opt. **42**, 6645 (2003).
[43] C. Pearman, C. Adams, S. Cox, P. Griffin, D. Smith, and I. Hughs, J. Phys. B **35**, 5141 (2002).
[44] A. Siegman, *Lasers* (Unversity Science Books, Sausalito, CA, 1986).
[45] D. M. Stamper-Kurn, Ph.D. thesis, Massachusetts Institute of Technology, 2000; http://cua.mit.edu/ketterle_group/Theses/thesis_DMSK.pdf
[46] IPG Photonics EAD and RLM series amplifiers.
[47] H. Moosmüller and J. Vance, Opt. Lett. **22**, 1135 (1997).
[48] J. Bienfang, C. A. Denman, B. W. Grime, P. D. Hillman, G. T. Moore, and J. M. Telle, Opt. Lett. **28**, 2219 (2003).
[49] R. J. Thompson, M. Tu, D. C. Aveline, N. Lundblad, and L. Maleki, Opt. Express **11**, 1709 (2003).
[50] S. Shang, B. Sheehy, P. van der Straten, and H. Metcalf, Phys. Rev. Lett. **67**, 1094 (1991).
[51] W. Ketterle, K. Davis, M. Joffe, A. Martin, and D. Pritchard, Phys. Rev. Lett. **70**, 2253 (1993).
[52] W. Ketterle and N. van Druten, in *Advances in AMO Physics*, edited by B. Bederson and H. Walther (Academic, San Diego, 1996), Vol. 37, p. 181; http://cua.mit.edu/ketterle_group/Projects_1996/Pubs_96/kett96_evap_preprint.pdf.
[53] W. Ketterle, D. S. Durfee, and D. M. Stamper-Kurn, in Bose-Einstein Condensation in Atomic Gases. *Proceedings of the International School of Physics "Enrico Fermi" Course CXL* (IOS, Amsterdam, 1999); cond-mat/9904034.
[54] Y. Castin and R. Dum, Phys. Rev. Lett. **77**, 5315 (1996).
[55] B. Borca, J. W. Dunn, V. Kokoouline, and C. H. Greene, Phys. Rev. Lett. **91**, 070404 (2003).
[56] J. Schuster, A. Marte, S. Amtage, B. Sang, G. Rempe, and H. C. W. Beijerink, Phys. Rev. Lett. **87**, 170404 (2001).
[57] E. A. Burt, R. W. Ghrist, C. J. Myatt, M. J. Holland, E. A. Cornell, and C. E. Wieman, Phys. Rev. Lett. **79**, 337 (1997).
[58] B. Tolra, K. O'Hara, J. Huckans, W. Phillips, S. Rolston, and J. Porto, Phys. Rev. Lett. **92**, 190401 (2003).
[59] D. Harber, H. Lewandowski, J. McGuirk, and E. Cornell, Phys. Rev. A **66**, 053616 (2002).
[60] A. Görlitz *et al.*, Phys. Rev. Lett. **90**, 090401 (2003).
[61] S. Inouye, M. Andrews, J. Stenger, H.-J. Miesner, D. Stamper-Kurn, and W. Ketterle, Nature (London) **392**, 151 (1998).
[62] J. Stenger, S. Inouye, M. Andrews, H.-J. Miesner, D. Stamper-Kurn, and W. Ketterle, Phys. Rev. Lett. **82**, 2422 (1999).
[63] A. Marte, T. Volz, J. Schuster, S. Durr, G. Rempe, E. G. M. van Kempen, and B. Verhaar, Phys. Rev. Lett. **89**, 283202 (2002).
[64] D. S. Durfee, Ph.D. thesis, Massachusetts Institute of Technology, 1999; http://www.physics.byu.edu/faculty/durfee/DSDThesis.pdf
[65] T. Bergeman, G. Erez, and H. J. Metcalf, Phys. Rev. A **35**, 1535 (1987).
[66] B. F. Melton and V. L. Pollak, J. Magn. Reson., Ser. A **122**, 42 (1996).
[67] D. Montgomery, *Solenoid Magnet Design; The Magnetic and Mechanical Aspects of Resistive and Superconducting Systems* (Wiley-Interscience, New York, 1969).
[68] C. Samuelis, E. Tiesinga, T. Laue, M. Elbs, H. Knockel, and E. Tiemann, Phys. Rev. A **63**, 012710 (2000).
[69] D. Steck, http://steck.us/alkalidata/rubidium87numbers.pdf (2002).
[70] H. Metcalf and P. van der Straten, *Laser Cooling and Trapping*, Graduate Texts in Contemporary Physics (Springer, New York, 1999).